

Urban Flow and Dispersion Simulation Using a CFD Model Coupled to a Mesoscale Model

JONG-JIN BAIK AND SEUNG-BU PARK

School of Earth and Environmental Sciences, Seoul National University, Seoul, South Korea

JAE-JIN KIM

Department of Environmental Atmospheric Sciences, Pukyong National University, Busan, South Korea

(Manuscript received 25 June 2008, in final form 21 January 2009)

ABSTRACT

Flow and pollutant dispersion in a densely built-up area of Seoul, Korea, are numerically examined using a computational fluid dynamics (CFD) model coupled to a mesoscale model [fifth-generation Pennsylvania State University–National Center for Atmospheric Research Mesoscale Model (MM5)]. The CFD model used is a Reynolds-averaged Navier–Stokes equations model with the renormalization group $k - \varepsilon$ turbulence model. A one-way nesting method is employed in this study. MM5-simulated data are linearly interpolated in time and space to provide time-dependent boundary conditions for the CFD model integration. In the MM5 simulation, four one-way nested computational domains are considered, and the innermost domain with a horizontal grid size of 1 km covers the Seoul metropolitan area and its adjacent areas, including a part of the Yellow Sea. The NCEP final analysis data are used as initial and boundary conditions for MM5. MM5 is integrated for 48 h starting from 0300 LST 1 June 2004 and the coupled CFD–MM5 model is integrated for 24 h starting from 0300 LST 2 June 2004. During the two-day period, a high-pressure system was dominant over the Korean peninsula, with clear conditions and weak synoptic winds. MM5 simulates local circulations characterized by sea breezes and mountain/valley winds. MM5-simulated synoptic weather and near-surface temperatures and winds are well matched with the observed ones. Results from the coupled CFD–MM5 model simulation show that the flow in the presence of real building clusters can change significantly as the ambient wind speed and direction change. Diurnally varying local circulations mainly cause changes in ambient wind speed and direction in the present simulation. Some characteristic flows—such as the double-eddy circulation, channeling flow, and vertical recirculation vortex—are simulated. Pollutant dispersion pattern and the degree of lateral pollutant dispersion are shown to be complicated in the presence of real building clusters and under varying ambient wind speed and direction. This study suggests that because of the sensitive dependency of urban flow and pollutant dispersion on variations in ambient wind, time-dependent boundary conditions should be used to better simulate or predict them when the ambient wind varies over the period of CFD model simulation.

1. Introduction

Flow in a densely built-up urban area and dispersion therein are quite complex because of the influence of buildings on flow and dispersion and unsteady meteorological conditions. To understand the fluid dynamics of such complex flow and dispersion and to better predict them, urban flow and dispersion have been extensively

studied through wind tunnel or water tank experiments, field observations, and computational fluid dynamics (CFD) model simulations, particularly focusing on flow and dispersion in street canyons (e.g., Kastner-Klein et al. 2001; Hanna et al. 2002; Chang and Meroney 2003; Liu et al. 2004; Eliasson et al. 2006; Di Sabatino et al. 2007; Flaherty et al. 2007; Li et al. 2008; Blocken et al. 2008). Building configurations in previous CFD modeling studies are diverse with specific research objectives, ranging from an idealized street canyon to a real urban setting. For example, Flaherty et al. (2007) numerically investigated flow and plume dispersion in Oklahoma City, Oklahoma, and showed that the many short buildings

Corresponding author address: Jong-Jin Baik, School of Earth and Environmental Sciences, Seoul National University, Seoul 151-742, South Korea.
E-mail: jjbaik@snu.ac.kr

have a relatively small effect on the flow field, whereas the few tall buildings considerably influence the transport and diffusion of tracer gas. A few review articles on urban flow and dispersion are available. Vardoulakis et al. (2003) reviewed air quality modeling in street canyons, Ahmad et al. (2005) reviewed wind tunnel studies on dispersion at street canyons and intersections, and Li et al. (2006) reviewed progress in CFD modeling of flow and dispersion in street canyons.

With advances in numerical modeling and the rapid increase in computing power, CFD models are now capable of simulating or predicting flow and dispersion in a real urban setting with a large computational domain and high horizontal and vertical resolutions. In this situation, appropriate boundary conditions should be given for realistic simulation or prediction. At present, data from routine observations in urban areas (radiosonde, meteorological tower, etc.) are temporally and spatially not fine enough to be used as boundary-condition data for CFD models. One way to cope with this problem is to couple a CFD model to a mesoscale model so that the mesoscale model provides time-dependent and spatially varying boundary conditions for the CFD model.

There are several studies that investigate flow or dispersion in built-up areas using CFD models with boundary conditions provided by mesoscale models. Ehrhard et al. (2000) simulated microscale wind field in an industrial area in Germany using a CFD model and a mesoscale model. They showed that the coupled model is capable of simulating the microscale wind field through the comparison of the measured and simulated wind speed and direction at many locations. In their study, the boundary conditions for the CFD model are not time varying. Brown et al. (2000) simulated the microscale wind field in downtown Salt Lake City, Utah, using two CFD models (one for urban scale and the other for building scale) and a mesoscale model [Coupled Ocean–Atmosphere Mesoscale Prediction System (COAMPS); Hodur 1997]. In their study, the vertical profiles of spatially averaged COAMPS data at a specific time are used to drive the urban-scale CFD simulation. Cox et al. (2000) presented preliminary results of contaminant transport over a short period in downtown Washington, D.C., using a CFD model and a mesoscale model (COAMPS).

In this study, we couple a CFD model to a mesoscale model [fifth-generation Pennsylvania State University–National Center for Atmospheric Research Mesoscale Model (MM5; Dudhia 1993; Grell et al. 1994)] and simulate flow and dispersion in a densely built-up area of Seoul, Korea, using the coupled model. Unlike the previous studies (Ehrhard et al. 2000; Brown et al. 2000; Cox et al. 2000), the CFD model is integrated for a

longer period (1 day) with time-varying boundary conditions provided by the mesoscale model. This allows us to examine the influences of time-varying mesoscale flows on microscale flow in an urban area and dispersion therein. This examination is a new attempt. In section 2, the CFD and mesoscale models, simulation setup, and coupling method are described. In section 3, the simulation results are presented and discussed. A summary and conclusions are given in section 4.

2. Model description, simulation setup, and coupling method

a. CFD model

As a CFD model, the Reynolds-averaged Navier–Stokes equations model with the renormalization group (RNG) $k - \varepsilon$ turbulence model developed by Kim and Baik (2004) is used in this study. The momentum equation, mass continuity equation, and transport equation of a passive scalar (e.g., pollutant) are expressed by

$$\frac{\partial U_i}{\partial t} + U_j \frac{\partial U_i}{\partial x_j} = -\frac{1}{\rho_0} \frac{\partial P^*}{\partial x_i} + \nu \frac{\partial^2 U_i}{\partial x_j \partial x_j} - \frac{\partial}{\partial x_j} (\overline{u_i u_j}), \quad (1)$$

$$\frac{\partial U_j}{\partial x_j} = 0, \quad \text{and} \quad (2)$$

$$\frac{\partial C}{\partial t} + U_j \frac{\partial C}{\partial x_j} = D \frac{\partial^2 C}{\partial x_j \partial x_j} - \frac{\partial}{\partial x_j} (\overline{c u_j}) + S_c, \quad (3)$$

where U_i is the i th mean velocity component, C is the mean pollutant concentration, u_i is the fluctuation from U_i , c is the fluctuation from C , P^* is the deviation of pressure from its reference value, ρ_0 is the air density, ν is the kinematic viscosity of air, and D is the molecular diffusivity of pollutant. The S_c in (3) denotes the source term of pollutant.

The Reynolds stress in (1) and the turbulent pollutant flux in (3) are parameterized using

$$-\overline{u_i u_j} = K_m \left(\frac{\partial U_i}{\partial x_j} + \frac{\partial U_j}{\partial x_i} \right) - \frac{2}{3} \delta_{ij} k \quad \text{and} \quad (4)$$

$$-\overline{c u_j} = K_c \frac{\partial C}{\partial x_j}. \quad (5)$$

Here, K_m is the eddy (or turbulent) viscosity of momentum, K_c is the eddy diffusivity of pollutant, k is the turbulent kinetic energy, and δ_{ij} is the Kronecker delta. In the RNG $k - \varepsilon$ turbulence model, K_m is represented by

$$K_m = \nu \left[1 + \left(\frac{C_\mu}{\nu} \right)^{1/2} \frac{k}{\varepsilon^{1/2}} \right]^2, \quad (6)$$

where C_μ is an empirical constant and ε is the dissipation rate of turbulent kinetic energy. Note that K_m in the RNG $k - \varepsilon$ turbulence model also includes molecular kinematic viscosity. It is calculated using k and ε that are prognostically computed with the equations of turbulent kinetic energy and its dissipation rate, given by

$$\frac{\partial k}{\partial t} + U_j \frac{\partial k}{\partial x_j} = -\overline{u_i u_j} \frac{\partial U_i}{\partial x_j} + \frac{\partial}{\partial x_j} \left(\frac{K_m}{\sigma_k} \frac{\partial k}{\partial x_j} \right) - \varepsilon \quad \text{and} \quad (7)$$

$$\begin{aligned} \frac{\partial \varepsilon}{\partial t} + U_j \frac{\partial \varepsilon}{\partial x_j} = & -C_{\varepsilon 1} \frac{\varepsilon}{k} \overline{u_i u_j} \frac{\partial U_i}{\partial x_j} + \frac{\partial}{\partial x_j} \left(\frac{K_m}{\sigma_\varepsilon} \frac{\partial \varepsilon}{\partial x_j} \right) \\ & - C_{\varepsilon 2} \frac{\varepsilon^2}{k} - R, \end{aligned} \quad (8)$$

where σ_k , σ_ε , $C_{\varepsilon 1}$, and $C_{\varepsilon 2}$ are empirical constants. The term R in (8) is included to account for nonequilibrium strain rates in the RNG $k - \varepsilon$ turbulence model (Yakhot et al. 1992). Here, K_c is calculated using K_m and a specified Schmidt number. The empirical constants in the RNG $k - \varepsilon$ turbulence model are specified following Yakhot et al. (1992) and Kim and Baik (2004). The governing equations in (1)–(3), (7), and (8) are numerically solved using a finite-volume method. Details of the numerical method are described in Baik et al. (2003).

b. Mesoscale model

As a mesoscale model, the nonhydrostatic, finite-difference model developed at Pennsylvania State University and the National Center for Atmospheric Research (Dudhia 1993; Grell et al. 1994) is used in this study. This model, called MM5, has been extensively and successfully used for atmospheric environmental applications as well as weather research and forecasting. MM5 provides many selective parameterization options for physical processes. In the present simulation using the MM5, version 3, cloud processes are represented with a simple ice microphysics scheme (Dudhia 1989) and the Kain–Fritsch cumulus parameterization (Kain and Fritsch 1993), radiative processes are represented with the Rapid Radiative Transfer Model (RRTM; Mlawer et al. 1997), and planetary boundary layer processes are represented with the Eta–Mellor–Yamada scheme (Janjić 1994) that calculates turbulent kinetic energy prognostically. Urban areas are treated using the urban-type dataset (e.g., a roughness length of 80 cm) among the 24-category land-use datasets in MM5.

c. Simulation setup

In the MM5 simulation, four one-way nested computational domains are considered with horizontal grid intervals of 27, 9, 3, and 1 km and respective time intervals of 81, 27, 9, and 3 s (Fig. 1a). The innermost domain covers the Seoul metropolitan area and its adjacent areas, including a part of the Yellow Sea (Fig. 1b). In each of the four domains, the horizontal grid dimension is 151×151 and the model top height is 100 hPa. There are 34 vertical layers in the outer three domains. Five additional layers are included in the innermost domain to provide a better resolution of the lower atmosphere close to the surface, hence providing more reliable boundary conditions for the CFD model. The National Centers for Environmental Prediction (NCEP) final analysis data, which are in 6-h intervals and have a horizontal resolution of $1^\circ \times 1^\circ$, are used as initial and boundary conditions in the MM5 simulation. The subgrid-scale cumulus parameterization is applied only in the outermost domain.

The CFD model domain ranges from $126^\circ 59' 6.5''$ to $126^\circ 59' 46.1''$ E and from $37^\circ 33' 44.2''$ to $37^\circ 34' 20.7''$ N (Fig. 1c). The horizontal grid interval is 9.72 m in the x direction and 11.31 m in the y direction, and the horizontal grid dimension is 102×102 . In the vertical, a nonuniform grid system with 62 layers is employed, in which the vertical grid interval is uniform with 5 m up to the 33rd layer, increases with an expansion ratio of 1.1 from the 34th layer to the 41st layer, and is then uniform with 10.72 m from the 42nd layer to the 62nd layer. The domain size is ~ 980 m in the x direction, ~ 1140 m in the y direction, and ~ 440 m in the z direction. The time step used is 1 s. The three-dimensional building configuration in the CFD model domain is depicted in Fig. 1c, and the horizontal cross-sectional areas of buildings at the surface are shown as shaded in Fig. 1d. Note that building structures smaller than the horizontal grid intervals of the CFD model are not resolved in the computational domain. The average building height is 24.3 m, and the fractional area covered by buildings at the surface (packing density) is 0.31.

This study selects a simulation case in which local circulations such as sea breezes and mountain winds under weak synoptic winds were well established in the Seoul metropolitan area (KMA 2004). We choose a 2-day period, 0300 LST 1–0300 LST 3 June 2004. MM5 is integrated for 48 h starting from 0300 LST 1 June 2004. The CFD model is integrated for 24 h starting from 0300 LST 2 June 2004, with initial and boundary conditions described in the next subsection.

d. Coupling method

To integrate the CFD model, initial and boundary conditions for the mean velocity (U_i) and turbulent kinetic

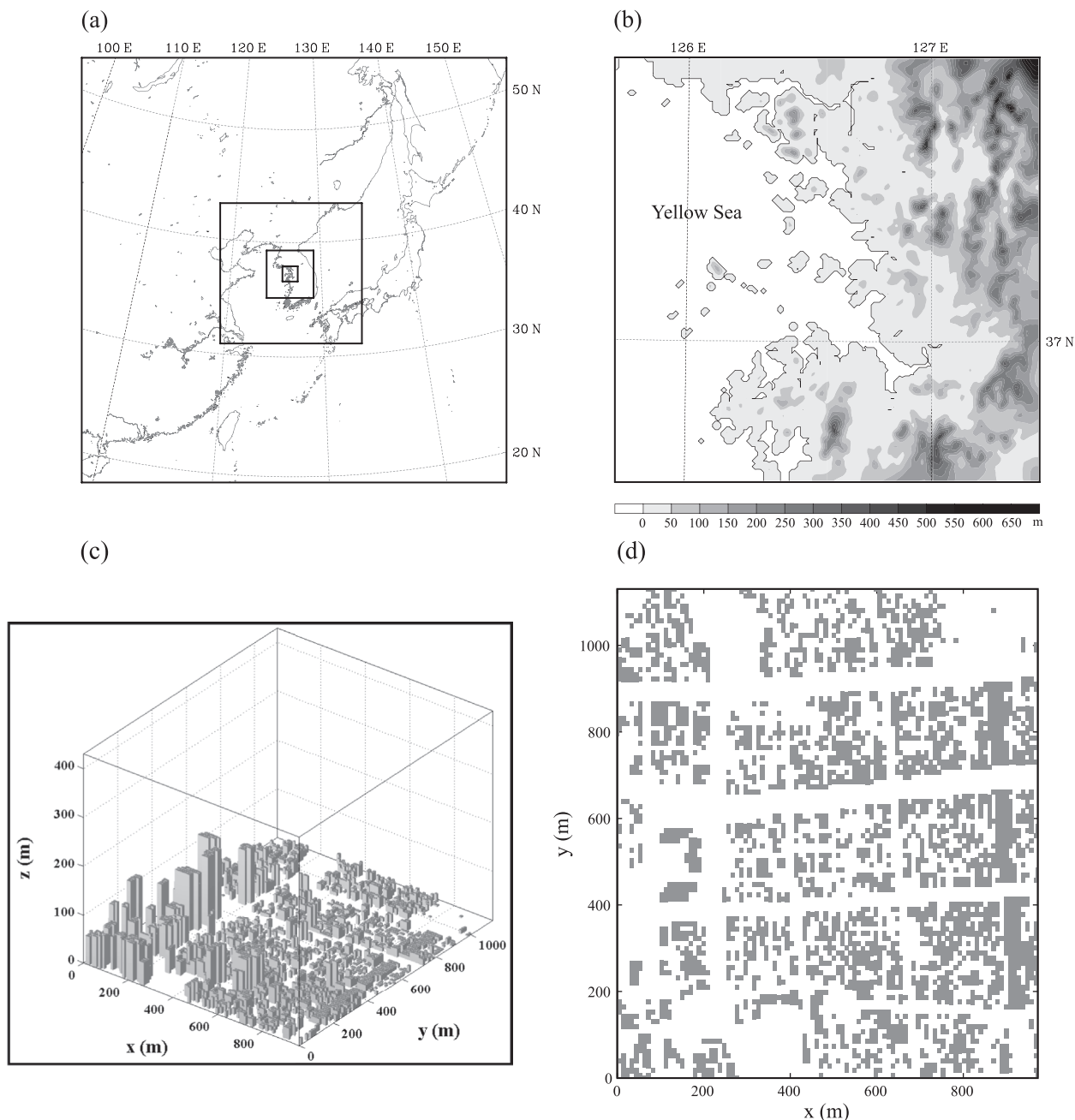


FIG. 1. (a) Nested computational domains in the MM5 simulation, (b) innermost MM5 domain with topography being shaded on a linear scale, (c) CFD model domain with three-dimensional building configuration, and (d) CFD model domain with horizontal building configuration at the surface.

energy (k) and its dissipation rate (ϵ) are needed. Here, it is noted that there are large differences in domain size and grid interval between the CFD model and MM5. The horizontal grid interval of the innermost MM5 domain is 1 km, which is about the horizontal domain size of the CFD model. In the present study, the location of the center of the CFD model domain is set to

coincide with that of a grid cell in the innermost MM5 domain, so information at only one grid cell from the MM5 simulation is actually used for the CFD model simulation (horizontal velocity components and turbulent kinetic energy). A one-way nesting method is employed to couple the CFD model to MM5. For this, MM5 is integrated first and MM5 simulation data are

saved in 10-min intervals. Then, these data are linearly interpolated in time and space (vertical direction) to provide inflow and top boundary conditions at every time step of the CFD model integration. Note that there are 10 MM5 vertical levels within the vertical domain of the CFD model. By linear interpolation, MM5 simulation data at the lowest 11 levels are used to make boundary conditions at 62 vertical levels in the CFD model simulation. At the outflow boundaries, a zero-gradient boundary condition is applied. The vertical velocity at the inflow boundary is specified to be zero. The dissipation rate of turbulent kinetic energy is not prognostically calculated in the MM5 simulation using the Eta–Mellor–Yamada scheme (Janjić 1994). Accordingly, in this study the dissipation rate of turbulent kinetic energy is diagnostically calculated following Kim and Baik (2004). For initial conditions, the CFD model is initialized by integrating it for 30 min with MM5-simulated inflow boundary conditions at $t = 0$ s (0300 LST 2 June 2004). This initialization is found to result in an adjusted quasi-steady wind field at $t = 0$ s in the CFD model domain.

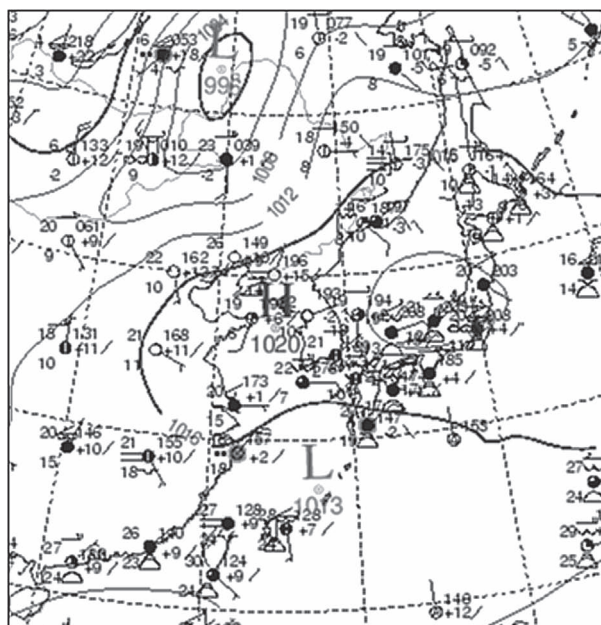
3. Results and discussion

a. Simulation with MM5

To examine how well MM5 simulates the selected case, the simulated synoptic weather is first compared to the observed one. Figure 2 shows the MM5-simulated sea level pressure field in the outermost domain at $t = 30$ h and the observed one at the corresponding time (0000 UTC 2 June 2004). At this time, the observed sea level pressure field exhibits a high-pressure system over the Korean peninsula, which extends in the east–west direction, and a low-pressure system north-northwest of the Korean peninsula, with the lowest sea level pressure of 996 hPa. These observed high- and low-pressure systems are reasonably well simulated using MM5, although the high-pressure system is somewhat stronger and wider in the simulation than in the observation.

Figure 3 shows the time evolution of simulated wind vector field at the lowest model level ($\sigma = 0.999$, about 7 m above the surface) in a subdomain of the innermost MM5 domain. The CFD model domain is marked by a square. At $t = 27$ h (corresponding to 0600 LST 2 June), the cool air moves down the mountain slopes. In the CFD model domain, a weak easterly wind blows. At $t = 31$ h (1000 LST), the land surface is heated by sunlight and valley winds appear. At $t = 35$ h (1400 LST), sea breezes blowing from the Yellow Sea toward the land are apparent in the western region. In the eastern region, the wind pattern is complicated because of the

(a)



(b)

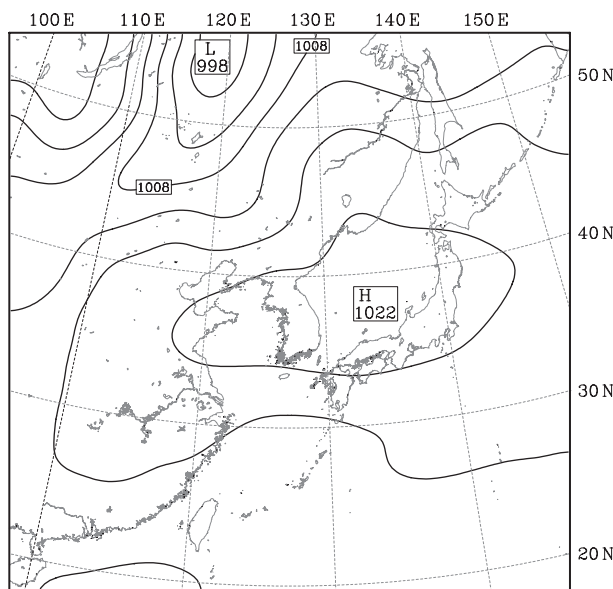


FIG. 2. (a) Observed sea level pressure field at 0000 UTC 2 Jun 2004 and (b) MM5-simulated sea level pressure field in the outermost domain at the corresponding time ($t = 30$ h). The contour interval is 4 hPa.

coexistence of sea breezes and valley winds in the presence of complex terrain. The CFD model domain experiences northwesterly wind. At $t = 39$ h (1800 LST), sea breezes penetrate farther inland and become well established. Westerly-northwesterly sea breezes are dominant over the entire domain. At $t = 43$ h (2200 LST), sea

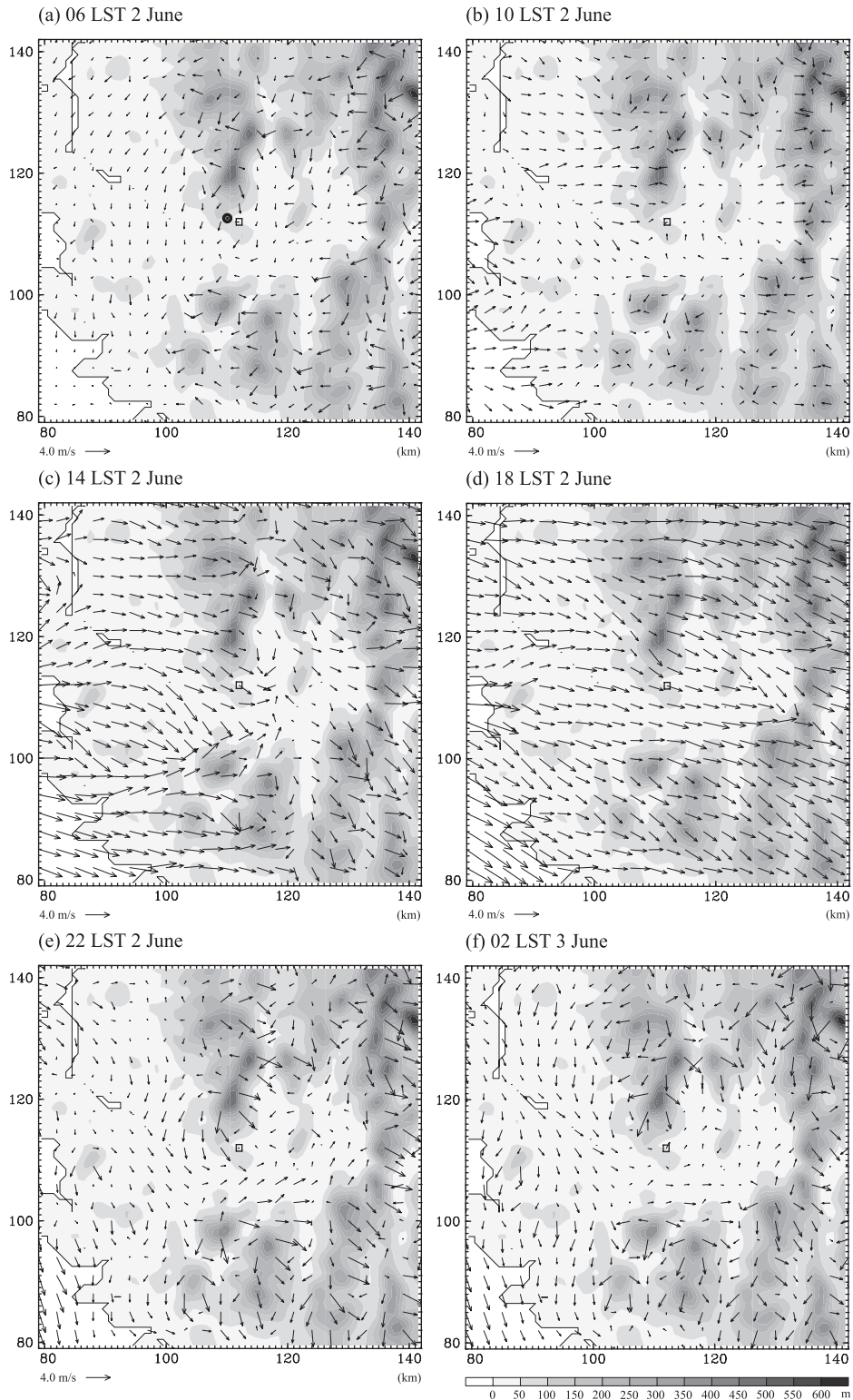


FIG. 3. Simulated wind vector fields at the lowest model level ($\sigma = 0.999$) in a subdomain of the innermost MM5 domain at $t =$ (a) 27 h (corresponding to 0600 LST 2 Jun), (b) 31 h (1000 LST), (c) 35 h (1400 LST), (d) 39 h (1800 LST), (e) 43 h (2200 LST), and (f) 47 h (0200 LST 3 Jun). Topography is shaded on a linear scale. The CFD model domain is indicated by an open square in each panel. The location of the Seoul meteorological observatory is indicated by the filled circle in (a).

breezes are almost absent and mountain winds appear. At this time, the wind is calm in the CFD model domain. At $t = 47$ h (0200 LST 3 June), mountain winds blow and a weak southwesterly wind is in the CFD model domain. The simulated circulations (Fig. 3) are typical of local circulations observed on clear late-spring and summer days when the synoptic wind is weak in the Seoul metropolitan area.

Figure 4 shows the time series of observed and MM5-simulated temperatures at $z = 1.5$ m. The surface observation was made at the Seoul meteorological observatory (marked by a filled circle in Fig. 3a), and the simulation data are taken at the MM5 grid point nearest to the observatory. An initial temperature difference between the observation and simulation is 4.6°C (cold bias). In this study, the NCEP final analysis data in a horizontal resolution of $1^{\circ} \times 1^{\circ}$ are interpolated to model grid points in the innermost MM5 domain, with a horizontal resolution of 1 km for its initial conditions. Noting that the observed urban heat island in Seoul is strong at 0300 LST (the initial time of MM5 integration; Kim and Baik 2005) and that the urban heat island effect is not properly reflected in the NCEP final analysis data, it is probable that a large difference in spatial scale at 0300 LST results in the large initial temperature difference to some or to a large extent. To reduce the initial temperature difference, assimilating available surface observation data for the Seoul metropolitan area, mainly from automatic weather stations, would be helpful. This topic needs to be investigated in a future work. It is observed from Fig. 4 that in the morning and early afternoon of the two-day simulation period, the simulated temperature is higher than the observed one. In the late afternoon and at night, the simulated temperature is lower than the observed one. This feature is also reported by Kondo et al. (2005). The simulated daily maximum temperature is 1–2 h ahead of the observed one. The root-mean-square error of the temperature in Fig. 4 is 2.7°C . Despite the above-mentioned deficiencies in the simulated temperature, the diurnal cycle of surface temperature is well simulated.

The version of MM5 used in this study does not contain an urban canopy parameterization, although some urban modeling studies have been undertaken using mesoscale models with urban canopy parameterization schemes (Martilli et al. 2002; Dupont et al. 2004; Otte et al. 2004; Kusaka and Kimura 2004; Holt and Pullen 2007). A recent numerical modeling study indicates that the nocturnal urban heat island in Seoul is enhanced when an urban canopy parameterization is included in a mesoscale model (Lee 2008). Therefore, it is speculated that the cold bias at night (Fig. 4) would be alleviated with the inclusion of an urban canopy parameterization.

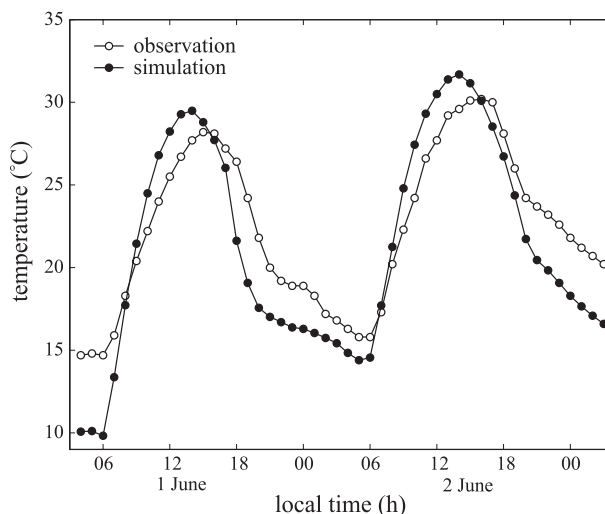


FIG. 4. Time series of observed and MM5-simulated temperatures at $z = 1.5$ m. The observation was made at the Seoul meteorological observatory, and the simulation data are taken at the MM5 grid point nearest to the observatory.

The time series of observed and MM5-simulated wind speeds and directions at $z = 10$ m are shown in Fig. 5. The observed wind speed exhibits a diurnal pattern that is especially associated with the sea-breeze circulation. The wind speed is strong in the late afternoon when the sea breeze is well developed. MM5 simulates the observed diurnal pattern of the wind speed well. The root-mean-square error of the wind speed is 0.8 m s^{-1} . The wind direction is also well simulated.

b. Simulation with a coupled CFD–MM5 model

1) FLOW ANALYSIS

The CFD model coupled to MM5 is integrated for 24 h starting from 0300 LST 2 June. Figure 6 shows simulated wind vector fields at $z = 2.5$ and 17.5 m. These are at $t = 11$ h, which corresponds to 1400 LST 2 June. The fractional area covered by buildings is 0.31 at $z = 2.5$ m and 0.12 at $z = 17.5$ m. The MM5-simulated ambient wind at $z = 2.5$ m is northwesterly and its speed is 1.4 m s^{-1} . In this study, the term ambient wind (ambient wind speed and direction) means the MM5-simulated wind for the CFD model domain. The MM5-simulated ambient wind at $z = 17.5$ m is also northwesterly, but its speed increases to 3.6 m s^{-1} . Complex urban flows are manifest in the presence of the real building clusters (Fig. 6). At $z = 2.5$ m, the simulated wind direction generally does not follow the ambient wind direction because of the influence of buildings on flows, except for the two void regions near the northern boundary ($\sim 220 \text{ m} < x < \sim 320 \text{ m}$ and $\sim 760 \text{ m} < x < \sim 980 \text{ m}$) where the simulated wind is parallel to the ambient wind.

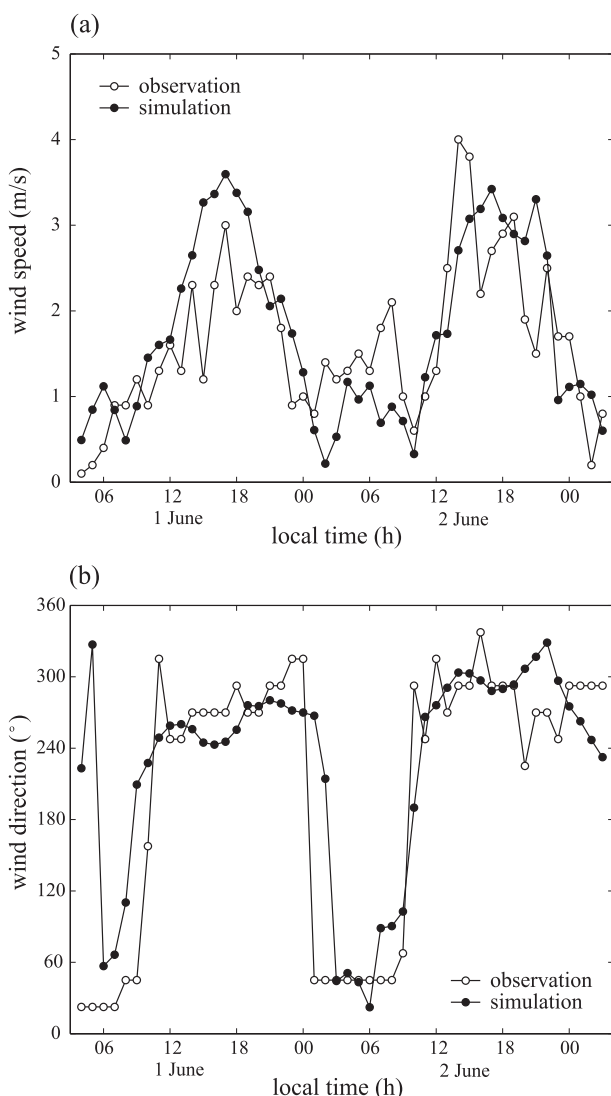


FIG. 5. Time series of observed and MM5-simulated (a) wind speeds and (b) wind directions at $z = 10$ m. The observation was made at the Seoul meteorological observatory, and the simulation data are taken at the MM5 grid point nearest to the observatory.

The simulated wind is strong in some regions around tall buildings (Fig. 1c). However, in most regions, the simulated wind speed is lower than the ambient wind speed, indicating that buildings act to retard wind speed. At $z = 17.5$ m, flows are strong and complex in some regions around tall buildings. In regions where buildings are sparse at this height, the northwesterly flow is dominant and a well-developed wake flow behind buildings is evident in many regions, in which there is little interference by other buildings.

The simulated wind vector fields for the three small regions indicated by rectangles in Fig. 6a are enlarged in Fig. 7 to clearly show some characteristic urban flow

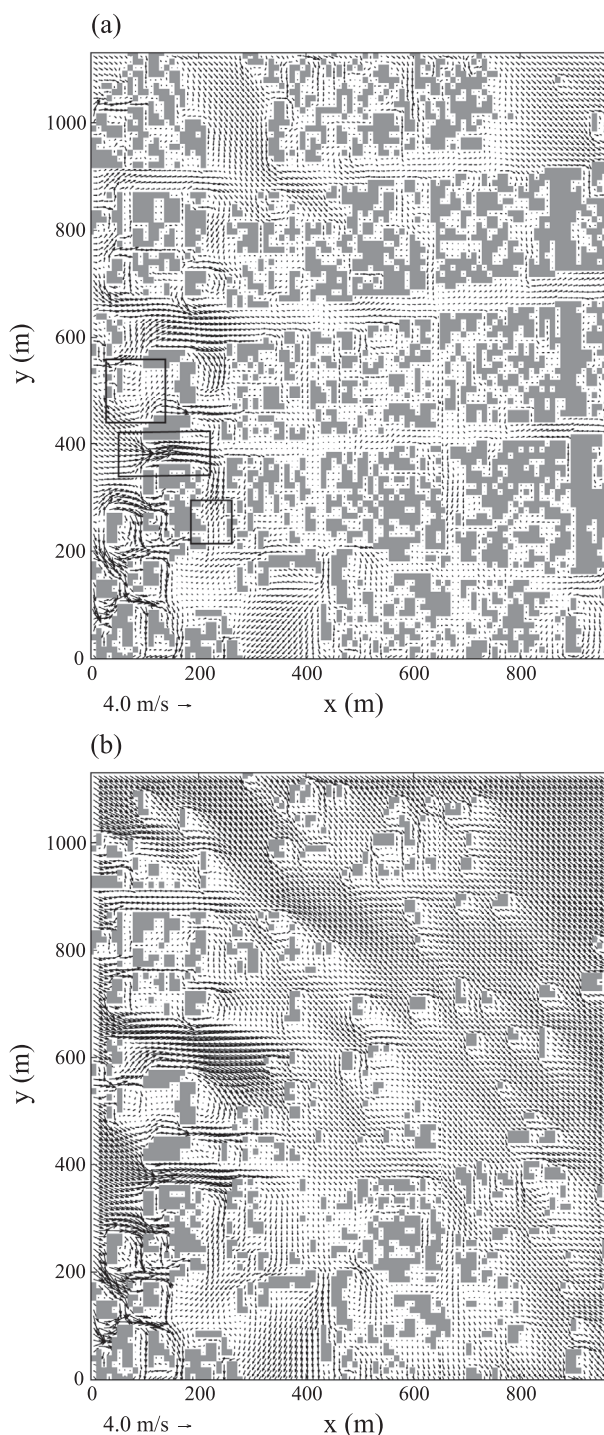


FIG. 6. Simulated wind vector fields at (a) $z = 2.5$ m and (b) $z = 17.5$ m at $t = 11$ h (corresponding to 1400 LST 2 Jun).

patterns. Figures 7a and 7b show horizontal wind vector fields at $z = 2.5$ m, and Fig. 7c shows the wind vector field in a horizontal plane of $z = 2.5$ m and in a vertical plane of $y = 254.4$ m. In Fig. 7a, the westerly flow

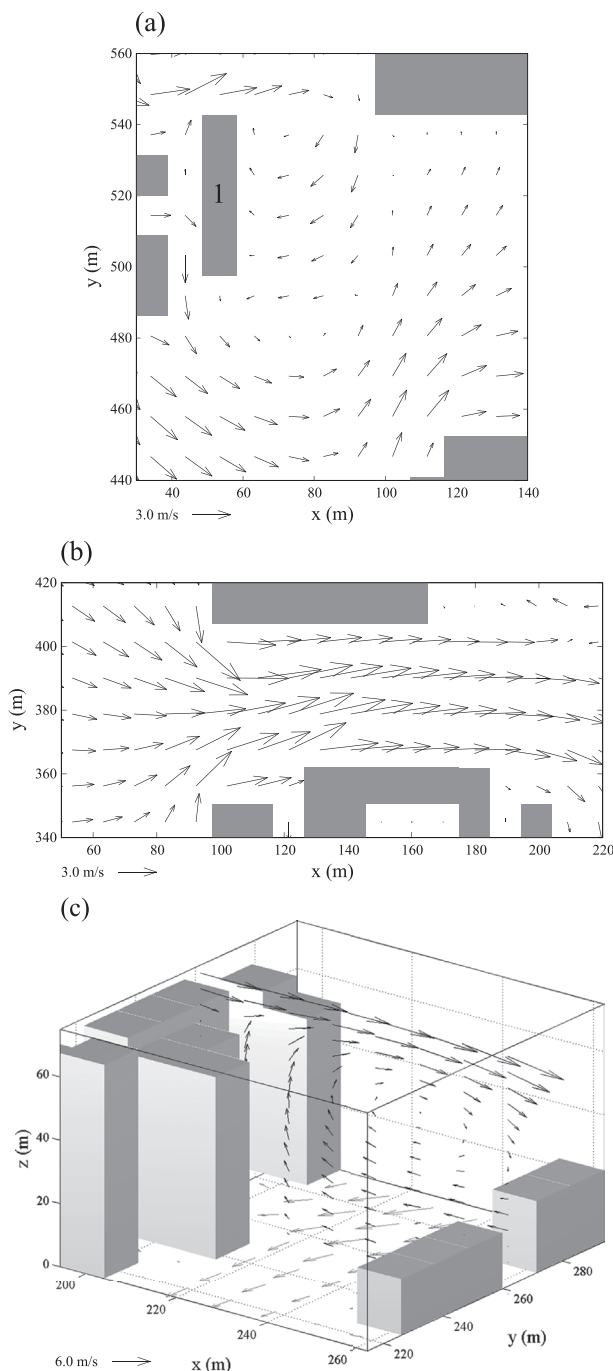


FIG. 7. Simulated wind vector fields in the three small regions (indicated by rectangles in Fig. 6a) at $t = 11$ h (corresponding to 1400 LST 2 Jun). Wind vectors fields in (a) and (b) are at $z = 2.5$ m, and (c) depicts the wind vector field in a horizontal plane of $z = 2.5$ m and in a vertical plane of $y = 254.4$ m.

toward the building elongated in the north–south direction (labeled 1 in Fig. 7a) at $y = 510$ m diverges northward and southward in front of the building. The northward flow is combined with the incoming flow near

the northern edge of the building, and a vortex rotating clockwise is formed behind the building. The southward flow is combined with the northwesterly inflow, and another vortex rotating counterclockwise is formed with its center at $x = 78$ m and $y = 486$ m. These two vortices are produced under the influence of the three buildings on the left, and the buildings on the right corners affect the size and intensity of the vortices to some extent. The simulated two counterrotating vortices in Fig. 7a resemble a double-eddy circulation formed behind a building (Hunter et al. 1992; Zhang et al. 1996). A typical channeling flow pattern is seen in Fig. 7b. Flows converge and strengthen near the entrance region of the channel-like street canyon formed by buildings, pass through the channel, and then leave it. The flow near the entrance region and in the channel region is stronger than the ambient wind. The strength of the horizontal flow at $x = 121$ m and $y = 379$ m is as high as 5.3 m s^{-1} , 3.8 times stronger than the ambient wind. Figure 7c exhibits a recirculation vortex in the vertical plane, which is formed behind the tall buildings on the left. The lower portion of the recirculation vortex is affected by the two short buildings on the right. At $z = 2.5$ m, the northeasterly flow enters this subregion (see Figs. 6a and 7c) and is combined with the recirculation vortex, producing a complex flow pattern there.

The simulated flow patterns in Fig. 7 are similar to those in a single-building configuration (double-eddy circulation and recirculation vortex) and in a simple-building configuration (channeling flow) but are different to some extent from idealized flow patterns because other adjacent buildings of various dimensions influence flows.

The MM5-simulated ambient wind speed and direction at $t = 23$ h (0200 LST 3 June) are 0.7 m s^{-1} and 211° at $z = 2.5$ m and 1.5 m s^{-1} and 212° at $z = 17.5$ m. The ambient wind is weaker at $t = 23$ h than at $t = 11$ h, and the ambient wind directions at the two times are different by about 90° . The characteristic flow patterns in the same three regions as in Fig. 7 are presented in Fig. 8. Weaker winds are simulated mainly because of weaker ambient wind. Figure 8a exhibits some southward flows around the elongated building (labeled 1) and a counterclockwise rotating vortex behind the upper-right building. A weak channeling flow is seen in Fig. 8b. In Fig. 8c, the flow impingement occurs at the frontal point (in the vertical plane) of the left building, and the flow diverges there. Some flows travel upward, whereas some flows travel downward, reach the street bottom, and then are directed downwind, forming a recirculation vortex. The vertical size of the recirculation vortex in Fig. 8c is smaller than that in Fig. 7c. It is noted that the general flow direction in the horizontal in Fig. 8b

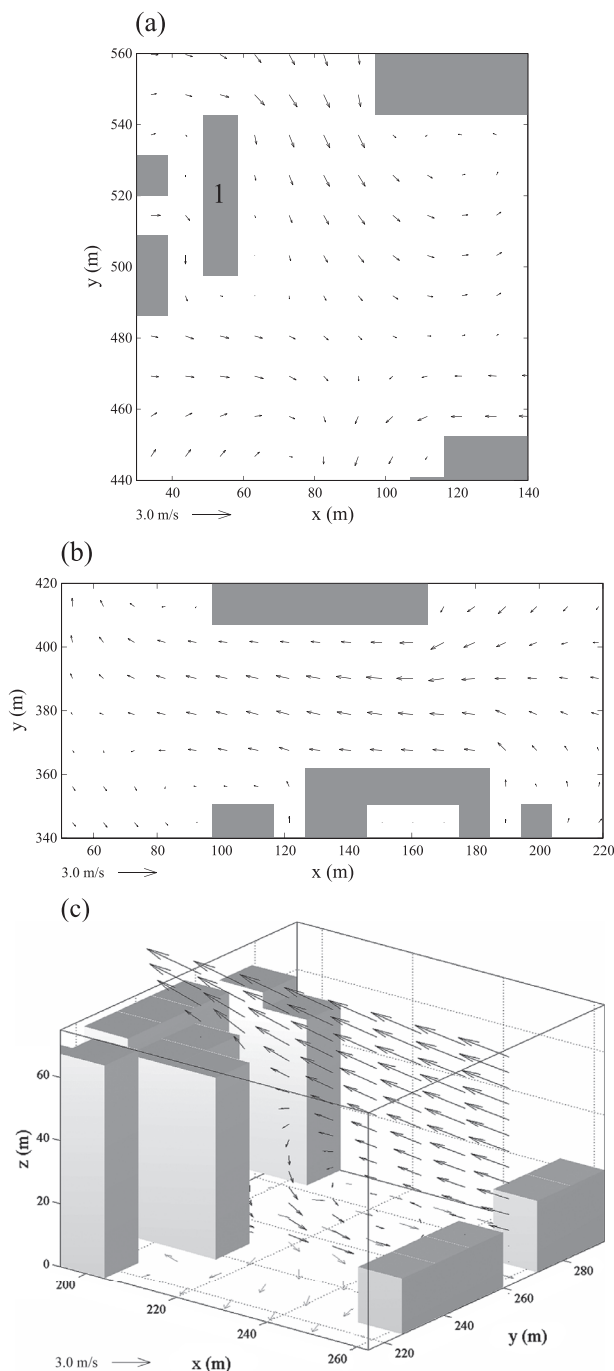


FIG. 8. As in Fig. 7 but at $t = 23$ h (corresponding to 02 LST 3 Jun).

(the general flow direction in the vertical in Fig. 8c) is opposite to that in Fig. 7b (Fig. 7c), although the ambient wind direction at $t = 23$ h differs from that at $t = 11$ h by about 90° .

Figures 6–8 clearly show that the urban flow in the presence of buildings can change significantly as the am-

bient wind speed and direction change. In the present study, changes in ambient wind speed and direction result mainly from diurnally varying local circulations (sea breezes and mountain/valley winds).

To examine the grid-interval dependency of the simulated flow field, two numerical simulations are performed with different grid intervals. The simulation setup is the same as that described in section 2, except that the grid interval in both the x and y directions is reduced by half in one simulation and the grid interval in the vertical is reduced by half in the other simulation. Figure 9 shows simulated wind vector fields in the small region (Fig. 7a) at $t = 11$ h (corresponding to 1400 LST 2 June) in the two simulation cases. These are at $z = 2.5$ m. The simulated wind field in the case of doubled horizontal resolution (Fig. 9a) is more distinctive than that in Fig. 7a. However, the characteristic flow patterns are very similar to each other, although there are slight differences in the positions of vortex centers. The simulated wind field in the case of doubled vertical resolution (Fig. 9b) closely resembles that in Fig. 7a. These results indicate that the grid intervals in the present study (Figs. 6–8) are adequate for capturing the gross features of urban flow in this study area. However, a finer grid resolution would be required to better resolve flows, especially near the buildings.

A typical integration time of CFD models used for urban flow and dispersion simulation is less than an hour or so with steady (not time dependent) boundary conditions (e.g., Brown et al. 2000). The mesoscale flows simulated in this study are diurnally varying, so the unsteady (time dependent) boundary conditions used for the present CFD model integration may be considered to vary slowly with time if the period of less than an hour or so is used for CFD model simulation. Hence, it is expected that CFD model-simulated urban flow obtained using steady boundary conditions for each case would be similar to that obtained using unsteady boundary conditions. To examine this issue, a numerical simulation is performed in which the CFD model is integrated for one hour, with steady boundary conditions provided by MM5 at the time corresponding to 1400 LST 2 June. A comparison is made between flow fields simulated using unsteady boundary conditions (Figs. 6 and 7) and those simulated using steady boundary conditions. We found (results not shown) that the simulated flow fields are overall similar to each other. This result implies that when the ambient wind varies little or does not change much over the period of CFD model simulation, steady boundary conditions could be approximately used. Even in this case, however, it would be better to use unsteady boundary conditions to better simulate or

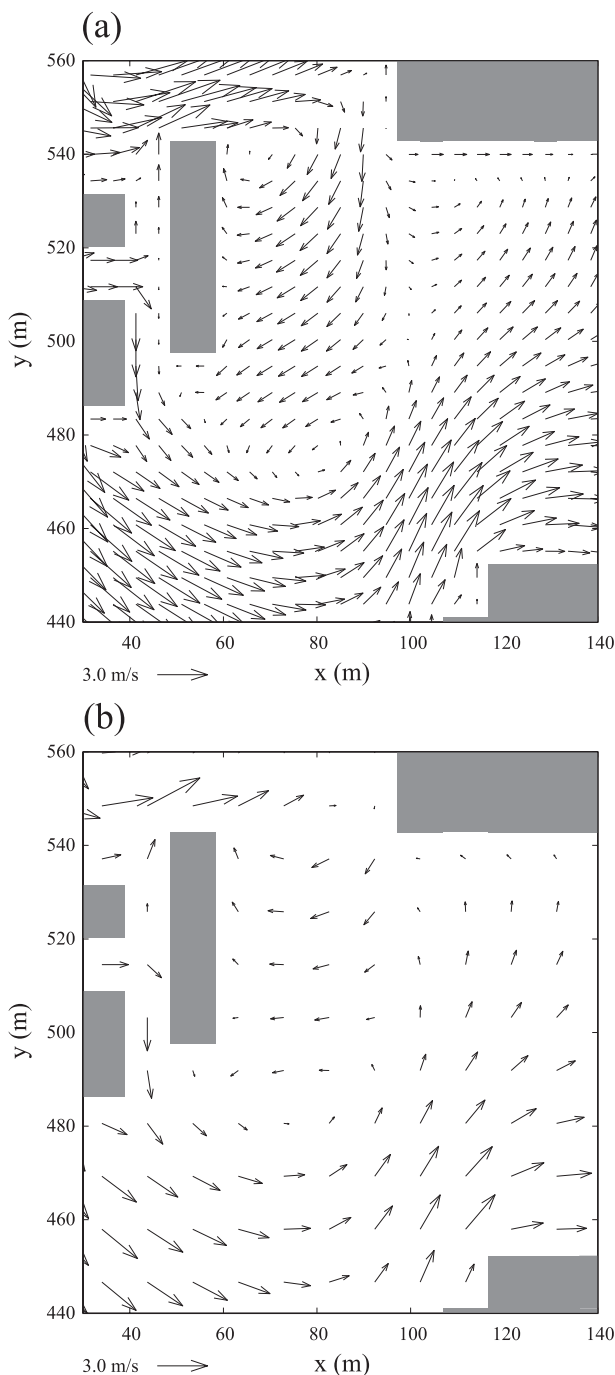


FIG. 9. Simulated wind vector fields in the small region (Fig. 7a) at $t = 11$ h (corresponding to 1400 LST 2 Jun) in the cases in which (a) the grid interval in both the x and y directions is reduced by half and (b) the grid interval in the vertical is reduced by half. These fields are at $z = 2.5$ m.

predict urban flow and dispersion. When the change in ambient wind over the period of CFD model simulation is not negligible, unsteady boundary conditions should be used.

2) DISPERSION ANALYSIS

In this subsection, the characteristics of urban dispersion are investigated in association with urban flow. For this, the transport Eq. (3) is simultaneously integrated for 6 h starting from 0900 LST 2 June. Passive pollutants are continuously emitted at a location of $x = 413$ m, $y = 650$ m, and $z = 2.5$ m. This location is chosen because characteristic pollutant dispersion patterns in the study area are well revealed within the computational domain, considering varying ambient wind over the period of the model simulation. The emission rate of pollutants is 10 ppb s^{-1} . Figure 10 shows pollutant concentration fields at $z = 2.5$ m at 1000, 1200, and 1400 LST 2 June, together with MM5-simulated ambient winds. At 1000 LST, a weak northeasterly ambient wind blows. The pollutant concentration is high just east of the source location. In that region, the CFD model-simulated wind is a weak southwesterly. A pollutant plume with concentrations higher than 1 ppb extends northwestward. These are features that cannot be deduced from the ambient wind direction alone. At 1200 LST, the westerly component of the ambient wind is large as the sea breeze develops. Pollutants are mainly dispersed eastward along the road oriented in the east–west direction. Along that road, the CFD model-simulated wind is mainly a relatively strong westerly. Also, weak pollutant dispersion is observed in the east–southeast direction. At 1400 LST, a strong northwesterly wind blows under the influence of the well-established sea breeze. The main direction of pollutant dispersion is largely parallel to the ambient wind direction. The different pollutant dispersion features at each time (Fig. 10) are caused by different ambient wind speeds and directions for the given building configuration.

Tominaga and Stathopoulos (2007) indicated that the optimal value of the Schmidt number ranges widely from 0.2 to 1.3, largely depending on local flow characteristics, and that the specific value selected influences prediction results significantly. They suggested that the Schmidt number should be determined by considering the dominant flow structure in each case. The Schmidt number in this study is specified as 0.9. Although the concentration field of the CFD model simulation with the Schmidt number of 0.9 for an idealized street canyon is in agreement with the wind tunnel data (Baik et al. 2003) and this value is equal to or not much different from values used in urban dispersion studies [see Table 1 of Tominaga and Stathopoulos (2007)], it is not certain whether this value is optimal for the real urban area. A field experiment could help to determine reliable and optimal Schmidt numbers for this area of Seoul.

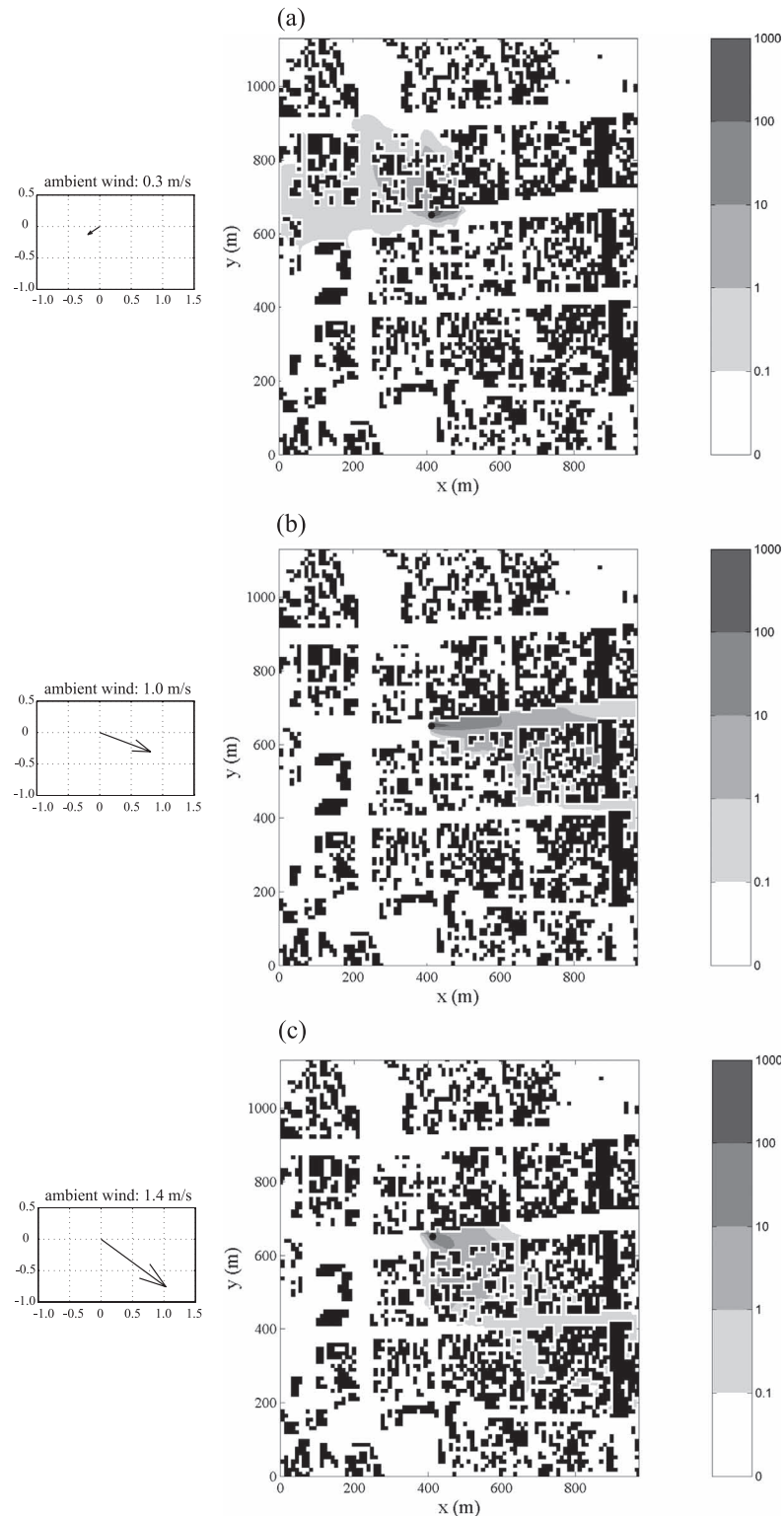


FIG. 10. Pollutant concentration fields (on a log scale) at $z = 2.5$ m at (a) 1000, (b) 1200, and (c) 1400 LST 2 Jun. The location of pollutant emission source is indicated by a filled circle, and the unit of pollutant concentration is parts per billion. The MM5-simulated ambient wind at each time is shown on the left.

To examine the degree of lateral pollutant dispersion in the presence of buildings, the following two parameters are introduced:

$$\bar{l} = \frac{\int Cl dl}{\int C dl} \quad \text{and} \quad (9)$$

$$\sigma_l^2 = \frac{\int C(l - \bar{l})^2 dl}{\int C dl}. \quad (10)$$

Here, \bar{l} represents the concentration-weighted lateral displacement of pollutant plume and σ_l is the concentration-weighted standard deviation of the lateral displacement of pollutant plume. For a steady-state Gaussian plume, $\bar{l} = 0$. Figure 11 shows the r axis and l axis at $z = 2.5$ m and 1400 LST 2 June. The r axis is parallel to the ambient wind direction at this height and time, and the l axis is perpendicular to the r axis. The coordinate origin is set to be the pollutant emission point. For a given r , the integrations in (9) and (10) are evaluated along a line parallel to the l axis.

Figure 12 shows the lateral displacement of pollutant plume (\bar{l}) and the standard deviation of the lateral displacement of pollutant plume (σ_l) as a function of r at $z = 2.5$ m at times corresponding to Fig. 10. At 1000 LST 2 June, the ambient wind is weak and northeasterly (Fig. 10a). The magnitude of the lateral displacement tends to be large as the distance from $r = 0$ increases. At $r = 200$ m, $\bar{l} = -192$ m. The lateral displacement is negative over the distance r , meaning that the concentration-weighted central line is displaced rightward from the r axis when looking at the downwind direction, as evident in Fig. 10a. The standard deviation changes very little with r . At 1200 LST, the ambient wind speed increases (Fig. 10b). The magnitude of the lateral displacement is smaller at 1200 LST than at 1000 LST. The standard deviation exhibits fluctuations over the negative r . The ambient wind speed further increases at 1400 LST (Fig. 10c). The lateral displacement (in its magnitude) and standard deviation are small as compared with those at 1000 and 1200 LST. Figure 12 indicates that the lateral displacement (in its magnitude) and standard deviation tend to become small as the ambient wind speed increases.

The parameters (9) and (10) provide clear physical meanings near the pollutant emission source region. However, as the distance from the pollutant emission point increases, the parameters might be not so meaningful because the pollutant plume can be significantly dispersed in the presence of complex buildings. So, the

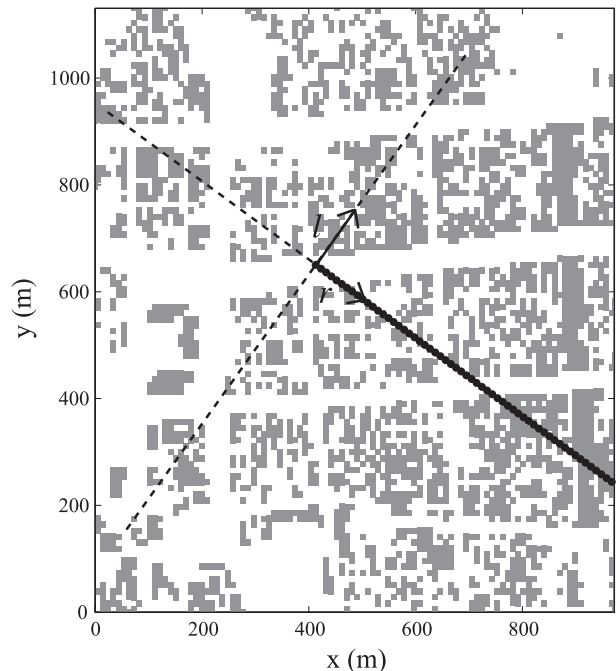


FIG. 11. The r axis and l axis at $z = 2.5$ m and 1400 LST 2 Jun. The r axis is parallel to the ambient wind direction, and the l axis is perpendicular to the ambient wind direction. The coordinate origin is the pollutant emission point.

results presented earlier (Fig. 12) are considered to be qualitative rather than quantitative. Further work is needed to characterize time-dependent pollutant dispersion plume in a more rigorous way.

4. Summary and conclusions

This study examined urban flow and pollutant dispersion in a densely built-up area of Seoul using a computational fluid dynamics model coupled to a mesoscale model (MM5). It was shown that the flow in the presence of real building clusters can change significantly as the ambient wind speed and direction change. It was also shown that the pollutant dispersion pattern and the degree of lateral pollutant dispersion are complicated in the presence of real building clusters and under varying ambient wind speed and direction. These results suggest that time-dependent boundary conditions should be used to better predict urban flow and dispersion using a CFD model and that a coupled CFD-mesoscale model can be reliably used for such a prediction.

Several problems remain to be solved. First, MM5-simulated temperature information was not used for the CFD model, although our CFD model now includes a thermodynamic energy equation. To treat thermal environment properly, temperatures at solid surfaces (street bottoms, building walls, and building roofs) should be

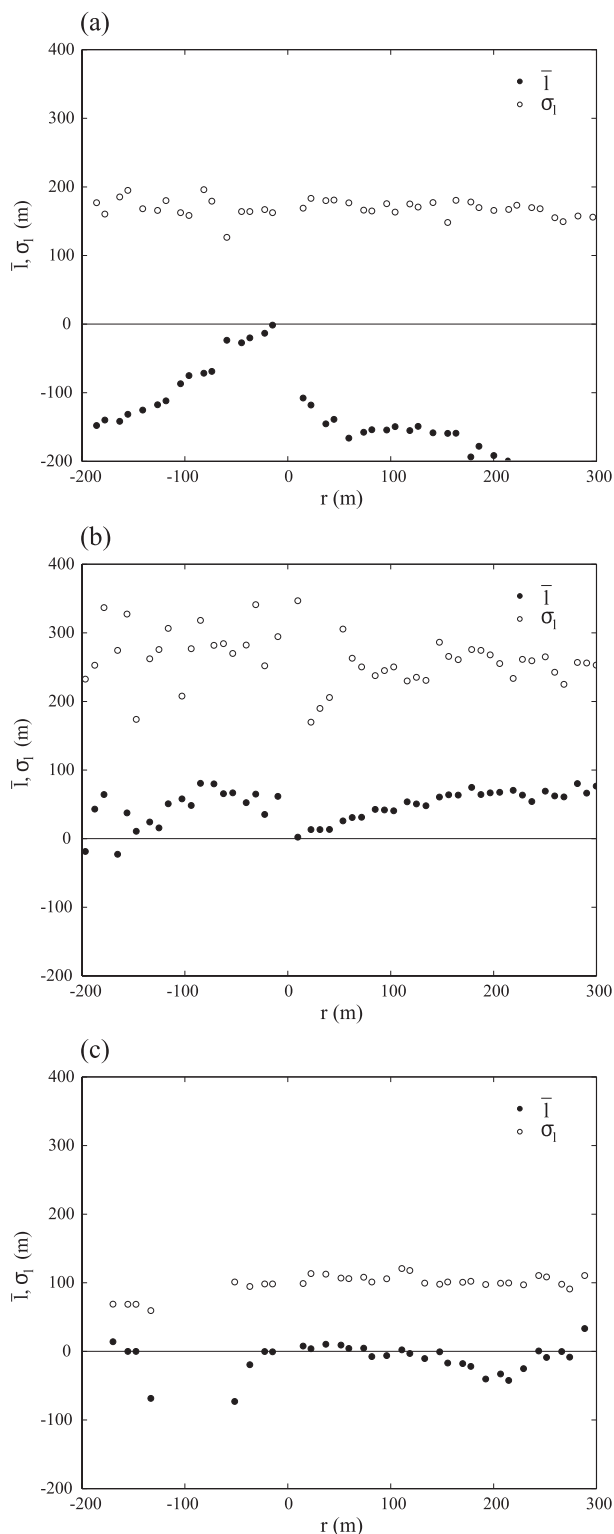


FIG. 12. The \bar{l} and σ_l as a function of r at $z = 2.5$ m at (a) 1000, (b) 1200, and (c) 1400 LST 2 Jun.

calculated. Because buoyancy plays an important role in determining urban flow and pollutant dispersion, that part needs to be implemented in the CFD model. Second, only information at one grid cell of MM5 was used for the CFD model. It is well known that MM5 often fails in simulating any phenomenon when the horizontal grid size is set to be very small (say, <1 km). At present, many sophisticated mesoscale models are available with which simulations with very high horizontal resolutions are feasible. The Weather Research and Forecasting Model is one of them. If such a model is employed, higher-resolution data (e.g., ~ 100 m) can be used as boundary conditions for the CFD model, thus making more realistic simulations. Third, the MM5 version that we used in this study does not contain an urban canopy parameterization. This should be included in a mesoscale model to better simulate mesoscale flows. We plan on dealing with these problems to develop a more reliable coupled CFD–mesoscale model for studying urban flow and pollutant dispersion.

Acknowledgments. The authors are very grateful to three anonymous reviewers for providing valuable comments on this work. This work was partly funded by the Korea Meteorological Administration Research and Development Program under Grant CATER 2006–2202.

REFERENCES

- Ahmad, K., M. Khare, and K. K. Chaudhry, 2005: Wind tunnel simulation studies on dispersion at urban street canyons and intersections—A review. *J. Wind Eng. Ind. Aerodyn.*, **93**, 697–717.
- Baik, J.-J., J.-J. Kim, and H. J. S. Fernando, 2003: A CFD model for simulating urban flow and dispersion. *J. Appl. Meteor.*, **42**, 1636–1648.
- Blocken, B., T. Stathopoulos, P. Saathoff, and X. Wang, 2008: Numerical evaluation of pollutant dispersion in the built environment: Comparisons between models and experiments. *J. Wind Eng. Ind. Aerodyn.*, **96**, 1817–1831.
- Brown, M., M. Leach, J. Reisner, D. Stevens, S. Smith, S. Chin, S. Chan, and B. Lee, 2000: Numerical modeling from mesoscale to urban scale to building scale. Preprints, *Third Symp. on the Urban Environment*, Davis, CA, Amer. Meteor. Soc., 8.1. [Available online at http://ams.confex.com/ams/AugDavis/techprogram/paper_15557.htm.]
- Chang, C.-H., and R. N. Meroney, 2003: Concentration and flow distributions in urban street canyons: Wind tunnel and computational data. *J. Wind Eng. Ind. Aerodyn.*, **91**, 1141–1154.
- Cox, C. F., B. Z. Cybyk, J. P. Boris, Y. T. Fung, and S. W. Chang, 2000: Coupled microscale-mesoscale modeling of contaminant transport in urban environments. Preprints, *Third Symp. on the Urban Environment*, Davis, CA, Amer. Meteor. Soc., 8.2. [Available online at http://ams.confex.com/ams/AugDavis/techprogram/paper_15208.htm.]

- Di Sabatino, S., R. Buccolieri, B. Pulvirenti, and R. Britter, 2007: Simulations of pollutant dispersion within idealised urban-type geometries with CFD and integral models. *Atmos. Environ.*, **41**, 8316–8329.
- Dudhia, J., 1989: Numerical study of convection observed during the Winter Monsoon Experiment using a mesoscale two-dimensional model. *J. Atmos. Sci.*, **46**, 3077–3107.
- , 1993: A nonhydrostatic version of the Penn State–NCAR mesoscale model: Validation tests and simulation of an Atlantic cyclone and cold front. *Mon. Wea. Rev.*, **121**, 1493–1513.
- Dupont, S., T. L. Otte, and J. K. S. Ching, 2004: Simulation of meteorological fields within and above urban and rural canopies with a mesoscale model (MM5). *Bound.-Layer Meteor.*, **113**, 111–158.
- Ehrhard, J., I. A. Khatib, C. Winkler, R. Kunz, N. Moussiopoulos, and G. Ernst, 2000: The microscale model MIMO: Development and assessment. *J. Wind Eng. Ind. Aerodyn.*, **85**, 163–176.
- Eliasson, I., B. Offerle, C. S. B. Grimmond, and S. Lindqvist, 2006: Wind fields and turbulence statistics in an urban street canyon. *Atmos. Environ.*, **40**, 1–16.
- Flaherty, J. E., D. Stock, and B. Lamb, 2007: Computational fluid dynamic simulations of plume dispersion in urban Oklahoma City. *J. Appl. Meteor. Climatol.*, **46**, 2110–2126.
- Grell, G. A., J. Dudhia, and D. R. Stauffer, 1994: A description of the fifth-generation Penn State/NCAR Mesoscale Model (MM5). NCAR Tech. Note NCAR/TN-398+STR, 138 pp.
- Hanna, S. R., S. Tehranian, B. Carissimo, R. W. Macdonald, and R. Lohner, 2002: Comparisons of model simulations with observations of mean flow and turbulence within simple obstacle arrays. *Atmos. Environ.*, **36**, 5067–5079.
- Hodur, R. M., 1997: The Naval Research Laboratory's Coupled Ocean/Atmosphere Mesoscale Prediction System (COAMPS). *Mon. Wea. Rev.*, **125**, 1414–1430.
- Holt, T., and J. Pullen, 2007: Urban canopy modeling of the New York City metropolitan area: A comparison and validation of single- and multilayer parameterizations. *Mon. Wea. Rev.*, **135**, 1906–1930.
- Hunter, L. J., G. T. Johnson, and I. D. Watson, 1992: An investigation of three-dimensional characteristics of flow regimes within the urban canyon. *Atmos. Environ.*, **26B**, 425–432.
- Janjić, Z. I., 1994: The step-mountain eta coordinate model: Further developments of the convection, viscous sublayer, and turbulence closure schemes. *Mon. Wea. Rev.*, **122**, 927–945.
- Kain, J. S., and J. M. Fritsch, 1993: Convective parameterization for mesoscale models: The Kain–Fritsch scheme. *The Representation of Cumulus Convection in Numerical Models*, Meteor. Monogr., No. 46, Amer. Meteor. Soc., 165–170.
- Kastner-Klein, P., E. Fedorovich, and M. W. Rotach, 2001: A wind tunnel study of organised and turbulent air motions in urban street canyons. *J. Wind Eng. Ind. Aerodyn.*, **89**, 849–861.
- Kim, J.-J., and J.-J. Baik, 2004: A numerical study of the effects of ambient wind direction on flow and dispersion in urban street canyons using the RNG $k-\epsilon$ turbulence model. *Atmos. Environ.*, **38**, 3039–3048.
- Kim, Y.-H., and J.-J. Baik, 2005: Spatial and temporal structure of the urban heat island in Seoul. *J. Appl. Meteor.*, **44**, 591–605.
- KMA, 2004: Monthly Weather Report, June 2004 (in Korean). Korean Meteorological Administration, 52 pp.
- Kondo, H., Y. Genchi, Y. Kikegawa, Y. Ohashi, H. Yoshikado, and H. Komiyama, 2005: Development of a multi-layer urban canopy model for the analysis of energy consumption in a big city: Structure of the urban canopy model and its basic performance. *Bound.-Layer Meteor.*, **116**, 395–421.
- Kusaka, H., and F. Kimura, 2004: Thermal effects of urban canopy structure on the nocturnal heat island: Numerical experiment using a mesoscale model coupled with an urban canopy model. *J. Appl. Meteor.*, **43**, 1899–1910.
- Lee, S.-H., 2008: Development of a vegetated urban canopy model and its application to urban heat island simulations. Ph.D. dissertation, Seoul National University, 185 pp.
- Li, X.-X., C.-H. Liu, D. Y. C. Leung, and K. M. Lam, 2006: Recent progress in CFD modelling of wind field and pollutant transport in street canyons. *Atmos. Environ.*, **40**, 5640–5658.
- , D. Y. C. Leung, and C.-H. Liu, 2008: Physical modeling of flow field inside urban street canyons. *J. Appl. Meteor. Climatol.*, **47**, 2058–2067.
- Liu, C.-H., M. C. Barth, and D. Y. C. Leung, 2004: Large-eddy simulation of flow and pollutant transport in street canyons of different building-height-to-street-width ratios. *J. Appl. Meteor.*, **43**, 1410–1424.
- Martilli, A., A. Clappier, and M. W. Rotach, 2002: An urban surface exchange parameterisation for mesoscale models. *Bound.-Layer Meteor.*, **104**, 261–304.
- Mlawer, E. J., S. J. Taubman, P. D. Brown, M. J. Iacono, and S. A. Clough, 1997: Radiative transfer for inhomogeneous atmospheres: RRTM, a validated correlated- k model for the longwave. *J. Geophys. Res.*, **102**, 16 663–16 682.
- Otte, T. L., A. Lacser, S. Dupont, and J. K. S. Ching, 2004: Implementation of an urban canopy parameterization in a mesoscale meteorological model. *J. Appl. Meteor.*, **43**, 1648–1665.
- Tominaga, Y., and T. Stathopoulos, 2007: Turbulent Schmidt numbers for CFD analysis with various types of flowfield. *Atmos. Environ.*, **41**, 8091–8099.
- Vardoulakis, S., B. E. A. Fisher, K. Pericleous, and N. Gonzalez-Flesca, 2003: Modelling air quality in street canyons: A review. *Atmos. Environ.*, **37**, 155–182.
- Yakhot, V., S. A. Orszag, S. Thangam, T. B. Gatski, and C. G. Speziale, 1992: Development of turbulence models for shear flows by a double expansion technique. *Phys. Fluids*, **A4**, 1510–1520.
- Zhang, Y. Q., S. P. Arya, and W. H. Snyder, 1996: A comparison of numerical and physical modeling of stable atmospheric flow and dispersion around a cubical building. *Atmos. Environ.*, **30**, 1327–1345.